Cassini INMS constraints on the composition and latitudinal fractionation of Saturn ring rain material

K.E. Miller [a,*], J.H. Waite Jr. [a], R.S. Perryman [a], M.E. Perry [b], A. Bouquet [c], B.A. Magee [d], B. Bolton [e], T. Brockwell [a], M.M. Hedman [f], C.R. Glein [a]

[a] Southwest Research Institute, San Antonio, TX, USA
[b] Johns Hopkins University Applied Physics Laboratory, Laurel, MD, USA
[c] Aix Marseille Univ, CNRS, CNES, LAM, Marseille, France
[d] Southwest Research Institute, Boulder, CO, USA
[e] Artistic Sciences Inc., San Antonio, TX, USA
[f] University of Idaho, Moscow, ID, USA

ARTICLE INFO

ABSTRACT

During Cassini's Grand Finale, the spacecraft flew between Saturn's upper atmosphere and its innermost ring, the D ring. Throughout these final orbits, Cassini encountered material flowing from the D ring into Saturn's atmosphere. Here, we present a compositional analysis of this material using data collected by Cassini's Ion Neutral Mass Spectrometer. We confirm the identification of CH_4, CO_2, CO, N_2, H_2O, NH_3, and organics in the ring material, and provide upper limits for organic compounds of interest. The H/C, O/C, N/C, and S/C ratios of ring material are constrained using three different kinds of model spectra: automated fits, hand fits of inorganics + hydrocarbons, and hand fits of inorganics + organics with priority given to O-, N-, and S-bearing organics. Additionally, we compare data from the final plunge to earlier orbits, and find that ring material can be divided into gas and dust constituents, with CO_2 at the volatility boundary between the two phases. At increasing distance above the equatorial plane, the gas/dust molar ratio increases.

1. Introduction

Constraining the composition of Saturn's ring rain[1] yields insight into the origin and evolution of the rings, as well as the effects on Saturn's atmospheric chemistry. Remote sensing observations of Saturn's rings provide spatially resolved compositional constraints for Saturn's main A, B, and C rings. These data suggest that water is the dominant constituent (Clark and McCord, 1980; Pilcher et al., 1970), and that the redness of the rings requires the presence of either organic material, frequently modeled using tholins as an analog (Cuzzi and Estrada, 1998; Cuzzi et al., 2018; Nicholson et al., 2008), or opaque minerals such as metallic iron or hematite (Clark et al., 2012).

Voyager data show that the A and B rings are both redder than the C ring, while the C ring has a darker spectrum (Estrada and Cuzzi, 1996). Subsequent modeling (Cuzzi and Estrada, 1998) of the anticipated spectral evolution of the rings due to influx of carbonaceous meteoroids

suggested that these heterogeneous compositional characteristics may be explained by the presence of intrinsic, red organic material (spectrally similar to tholin), and the addition of dark, neutral carbonaceous material (spectrally similar to amorphous carbon).

Comparative analysis of VIMS mosaics of the rings supported the modeled compositional heterogeneity, with an enhanced concentration of the "broad-band" and "UV" absorbers, which may be organic, in the C ring (Hedman et al., 2013). Filacchione et al. (2014) analyzed the VIMS spectral slope between 0.35 and 0.55 μm, which is indicative of intraparticle-intramolecular mixing of the darkening agent, and the slope between 0.55 and 0.95 μm, which indicates mixing of darkening materials at the grain size scale, as a function of radial distance from Saturn in the rings. They found that the C ring spectral features were consistent with an enhancement relative to the A and B rings of darkening material at the grain size scale.

Ciarniello et al. (2019) performed spectral modeling of the rings, and

---

found that the spatial distribution of the spectral characteristics are consistent with an intrinsic tholin-like material and an extrinsic darkening material. Both components were more abundant in the C ring than in the A or B rings, with a maximum total of approximately 10% by volume non-icy material. Model fits to HST-STIS data yield similar organic content (Cuzzi et al., 2018). For an upper limit organic density of 2.2 g cm^{-3} and ice density of 0.93 g cm^{-3}, this is equivalent to approximately 20% by mass organic material.

While infrared and shorter wavelengths only probe the ring particle surface, microwave radiation penetrates to much greater depths. Zhang et al. (2017a, 2017b) utilized this property to study the bulk composition of the ring particles with Cassini microwave observations. They reported 1 to 2% by volume non-icy material for most regions in the C ring, with up to 11% non-icy material in the middle C ring (Zhang et al., 2017b). They suggested that silicates are the candidate material that best fit data in the visible and near-IR regions at the abundances suggested by data at longer wavelengths. In contrast, microwave data from the A and B rings are consistent with 0.2 to 0.3% by volume non-icy material (Zhang et al., 2017a). These studies strongly suggest that the C ring has a higher proportion of non-icy material than the A and B rings do.

The Cassini mission provided remote sensing constraints on the D ring as well. Spectra from the D ring indicate the presence of water ice in the D72 and D73 ringlets as well as a red slope; methane was not identified (Hedman et al., 2007). Bright clumps in the D68 ringlet interior to D72 and D73 have been identified as the possible source for the material measured during the Grand Finale (Hedman, 2019; Waite et al., 2018). Most of the material in the D ring, and especially in D68, may be comprised of sub-10-µm particles (Hedman et al., 2007). Later model fits to the D68 scattering phase function suggest the particle size distribution is dominated by grains between 5 and 390 µm (Hedman and Stark, 2015). Notably, the model fits suggest water ice fractions <30% by volume, and the single best fit corresponds to a composition of 10% water and 90% iron-rich orthopyroxene by volume (Hedman and Stark, 2015). If we assume 10–30 vol% water with the remainder corresponding to ferrosilite (density ~3.95 g cm^{-3}), this corresponds to 3–9% water and 91–97% silicate by mass. Remote sensing constraints could therefore suggest that D68 is water-depleted relative to the main rings. However, it is also possible that irregularly shaped particles, which were not accounted for in the Hedman and Stark (2015) model fits based on spherical particles, caused the non-icy fraction of the grains to be overestimated.

For its Grand Finale, Cassini completed 22 orbits that took the spacecraft between Saturn and its rings, resulting in unprecedented in situ data on the chemistry of this region. These orbits followed a trajectory from north to south across the ring plane, with a closest approach at approximately 6° S latitude for the final five orbits (288-292). During these maneuvers, the spacecraft encountered material concentrated at the equator and flowing in to Saturn's atmosphere (Waite et al., 2018), as well as silicate and ice grains with larger sizes (Perry et al., 2018) and a broader latitudinal spread (Hsu et al., 2018). This material is hypothesized to originate from the rings, and to flow into the atmosphere from the D ring via collisional momentum transfer with Saturn's extended atmosphere (Mitchell et al., 2018; Perry et al., 2018). In situ measurements in Saturn's upper atmosphere of material from the D ring are consistent with the presence of abundant (~35% by mass) organic material in nanometer-scale particles measured by Cassini's Ion Neutral Mass Spectrometer (INMS) (Waite et al., 2018). The calculated influx rate for the smallest particles is on the order of 10^4 kg/s, which would imply depletion of the D ring on timescales of 10^3–10^4 years if continuous (Waite et al., 2018).

Here, we report constraints from INMS on the composition of these D ring nanoparticles and their associated volatiles. In Section 2, we present compositional constraints from the ring-crossing orbits. The natural mixture of compounds encountered produces a complex mass spectrum. In addition to ionization fragmentation that occurs in the electron

impact ion source in all INMS datasets (hereafter referred to as "ionization fragmentation" or "electron impact ionization fragmentation"), the high velocity of Cassini relative to the ring material during the Grand Finale resulted in impact fragmentation of nanoparticles in the antechamber leading to the ion source (hereafter, "impact fragmentation"). In recognition of these effects, we present both the molecular compounds identified from the spectra as well as the elemental ratios calculated from the model fits, which are still characteristic of the original ring material even in the case of possible chemistry inside the antechamber. In Section 2.1, we briefly describe the data processing and instrumental effects that are important to interpretation, namely adsorption and chemistry that may have occurred in the instrument due to the high velocity of the spacecraft. We then present the results of spectral deconvolution, including both identifications of molecular compounds and elemental ratios, in Section 2.2. The implications are discussed in Section 2.3, as well as constraints on impact fragmentation effects.

The trajectory of the Cassini spacecraft took it through the ring plane for its last complete orbits (288-292) before the final plunge (293). Simultaneous changes in altitude and latitude make study of the separate effects of these two variables on the dataset challenging. However, for the final plunge (293), the spacecraft terminated its orbit at approximately 11°N, and did not cross the ring plane. This change in trajectory allows us to test for latitudinal dependence in the composition of the inflowing material. In Section 3, we compare the ring-crossing orbits with the final plunge to study the effect of latitude. The methodology behind analysis of the latitudinal dependence is described in Section 3.1. Since the descent of the spacecraft during the final plunge was more rapid than the inbound descent for other orbits, modeling of adsorption effects is necessary to interpret comparisons between the orbits. This work is described in Section 3.2, while results are described in Section 3.3. Implications are discussed in Section 3.4. Finally, we present a summary of our conclusions in Section 4.

2. Compositional constraints

2.1. Data processing

The current study utilizes data from the closed source neutral (CSN) mode of INMS (Waite et al., 2004). Use of the closed source is necessary for the present analysis because of the CSN higher sensitivities as well as the limitations that the high velocity of the spacecraft places on the measurable energy range for the open source. Furthermore, open source neutral (OSNB) data were only obtained on orbit 291, and ring material was not detected above the background level. While use of the closed source data is necessary for these reasons, CSN data require significant processing because of interactions between the analyte and the closed source antechamber. Previous work identified both the adsorption of analyte molecules to the walls of the antechamber and the reaction of oxygen bearing compounds such as water with ice-grain-sputtered titanium (Magee et al., 2009; Teolis et al., 2010; Waite et al., 2006). These phenomena affect a range of molecules, but are particularly important for O-bearing molecules such as water, which is the most affected compound. The time-dependent signal for affected compounds appears delayed relative to other compounds (see Fig. S1), which without correction during data processing and analysis may result in artificially reduced mixing ratios for these "sticky" molecules near periapsis.

To mitigate the effects of this timing lag on calculation of the true mixing ratios, integration over the closest approach time segment is required. This integration requires the assumption that the ring inflow composition is essentially constant as a function of altitude, latitude, and time. While latitudinal effects on composition have been identified (see Section 3), the first order assumption of a constant composition is reasonable because the integrated spectrum is strongly dominated by the signal at closest approach (CA), which was relatively close to the ring plane and therefore is less compositionally fractionated. We create an

integrated spectrum for each flyby using the average signal for each mass over the full time period for which the 18 u signal (dominated by water, which exhibits the strongest adsorption effects) is above the background levels. Creation of the integrated spectra incorporates several data processing steps, including subtraction of the background and radiation counts (Perry et al., 2010), and is based on methods established for INMS Titan data (Magee et al., 2009). A detailed description of the data processing is provided in the Supplement. For this study, integrated spectra were generated for Proximal orbits 290 through 293 (hereafter ProxXXX). While the spacecraft trajectories in Prox288 and Prox289 were similar to those in Prox290 through 292, integrated spectra cannot be created for these orbits. In Prox288, incorrect coadding of data after the CA time window prevents calculation of an integrated spectrum. (However, Prox288 data during CA are appropriate for other analyses that do not require an integrated spectrum.) For Prox289, only a limited subset of masses was measured.

Ionization fragmentation results from decomposition of the parent molecule following the input of excess energy by the ionization process. Thus, electron impact ionization leads to the formation and detection of multiple masses from a single molecular analyte. The mass and relative intensity of the daughter fragments create a pattern that can be used as an identifier for the parent molecule. However, measurement of a complex natural environment without previous separation of compounds leads to superposition of these different daughter fragments, requiring deconvolution during data analysis for identification of the parent compounds.

For the present work, mass spectral modeling to deconvolve the ionization fragments was performed using a combination of fragmentation patterns from the INMS calibration unit and the NIST mass spectral library (see Acree and Chickos, 2019) for the remaining species. While NIST fragmentation patterns are not an exact description of INMS ionization responses, the similar electron impact ionization energies used (71 eV for INMS and 70 eV for NIST) make the NIST spectra a plausible proxy when calibrated values are not available (Magee et al., 2009).

Two different fitting methods were utilized here: "hand fits" and "auto fits." These methodologies differed in the criteria used for selecting the order of addition for each compound, which determines prioritization for attribution of the signal. For the hand fits, the order of compounds was selected within the context of knowledge of the environment sampled by the spectra. The hand fits were further divided into two categories that were designed to produce endmember models in terms of elemental ratios: hydrocarbons (HC) and O-,N-,S-rich (ONS).

For the auto fits, compounds were categorized into one of two lists, which were randomly sampled by a fitting routine. The first list contained the compounds identified in Waite et al. (2018), which can be included in the model with a high degree of certainty: CH_4, CO_2, CO, N_2, H_2O, and NH_3. The second list contained all molecular compounds in the NIST spectral library with a mass <100 u, in total 1996 compounds. Auto fit models excluded 1 u because of the possible contributions of the zero blast, which is a common problem in quadropole mass spectrometers. Further details on the fitting routines as well as on subsequent conversion from counts to number densities are provided in the Supplement.
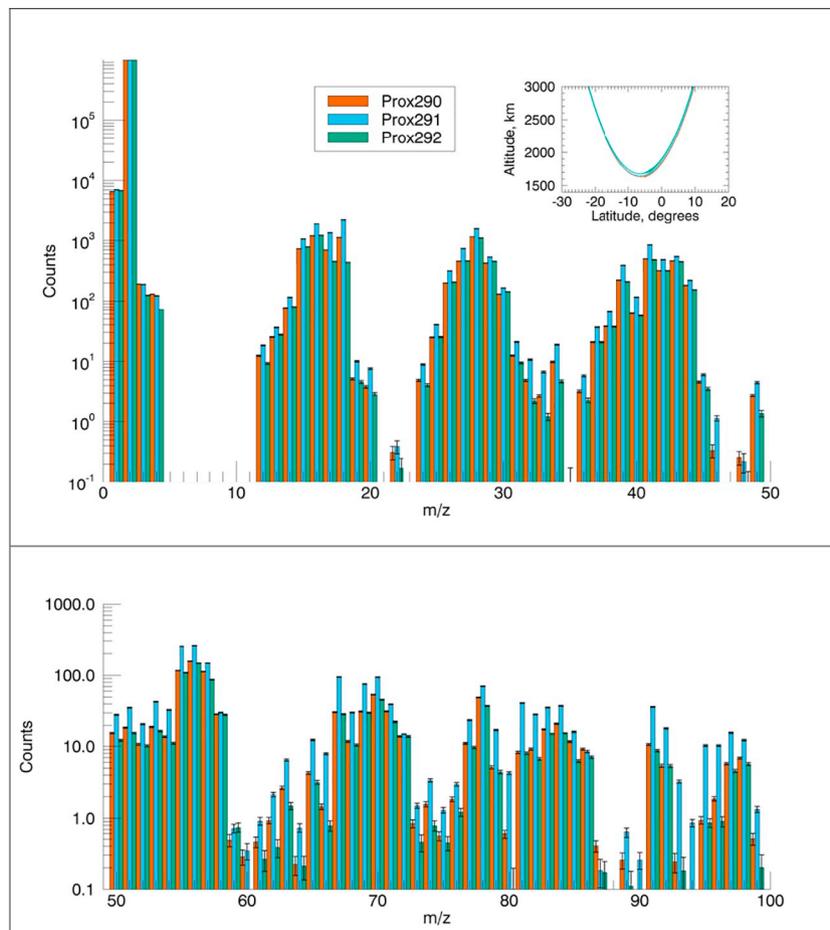

Fig. 1. Comparison of integrated spectra for Prox290, Prox291, and Prox292 scaled to 2 u. All three spectra were collected over similar altitudes, latitudes, and local time of day, as shown by the inset. In general, Prox290 and Prox292 are nearly identical within error, while Prox291 differs.

2.2. Results

A side-by-side comparison of the full integrated spectra (inbound and outbound) for Prox290, Prox291, and Prox292 is presented in Fig. 1. Spectra have been scaled to match at 2 u. Spectra in Fig. 1 show complex chemistry in the region sampled, with signal detected across the full range of masses measured (1 u to 99 u). While the general shape of the spectra from all three orbits is similar, Prox291 noticeably differs from Prox290 and Prox292 at several masses, suggesting some variability in the ring material composition. Since all three of these orbits had similar altitude and latitude profiles (see Fig. 1 inset), and were all collected at approximately noon local time, these differences are likely due to either longitudinal or temporal variation. Orbits were separated from one another by ~6.5 days, and were collected at different longitudes (given for CA in east longitude): 160° for Prox290, 326° for Prox291, 130° for Prox292, and 306° for Prox293 (the final plunge).

Hand fit model spectra using both the HC and ONS methodologies were produced for Prox290 through Prox292, for a total of six hand fit model spectra (Fig. S2). Based on these model spectra, overall ranges in elemental ratios and mixing ratios were calculated for the sampled material from the D ring. The ten compounds with the highest average mixing ratios from these fits are summarized in Table 1. These compounds include a mixture of inorganic volatiles such as NH_3, CO, and N_2, as well as organic compounds, most with molecular masses below 60 u. A more complete list of mixing ratios for the hand fit compounds is reported in Table S4. Note that O-, N-, and S-bearing organics were intentionally excluded from three of the model fits (the HC models).

In addition, 6000 auto fit spectra were generated for each integrated spectrum. The most abundant compounds for auto fits are summarized in Table 2. Similar to the hand fit models, these fits include a mixture of inorganic and organic compounds dominated by light molecules. Hydrogen, helium, water, methane, and ammonia are identified in Tables 1 and 2 as amongst the most abundant compounds for all model spectra. The mixing ratios calculated by each fit method are similar for all compounds, with the largest difference of ~25% for ammonia. These same five compounds are also identified as having high fit frequencies for the auto fits. Mixing ratios reported in Tables 1, 2 and S4 are with respect to the bulk composition measured by INMS. These tables report the preferred mixing ratio values for the exosphere composition, including constituents from Saturn's atmosphere below as well ring rain from above, and account for adsorption effects in the INMS closed source.

For comparison to compositional data given in Waite et al. (2018), Table 3 provides the mass percentages from the auto fits with respect to the hypothesized ring material (i.e. excluding H_2 and He). Since the "organic" category in Waite et al. (2018) included all counts that were not attributed to other compounds, we assume the same weight percent of organics here. Similar to Waite et al. (2018), these mass percentages are calculated using diffusion cross sections from the average auto fit mixing ratios. While the mixing ratios provide a measurement of the average composition of atmosphere plus ring particles, the mass

percentages account for fractionation in the atmosphere of the ring particle constituents and provide more accurate constraints on the composition of particles in the D ring. The CO_2 abundances from both this work and Waite et al. (2018) are the same within uncertainty. CH_4 and H_2O are both reduced in this analysis, while CO + N_2 and NH_3 are greater.

Elemental ratios for the ring particles were calculated from mixing ratios from the model fits according to three categories: the bulk composition that includes both inorganic (NH_3, H_2O, etc.) and organic compounds, the organic composition (here defined as compounds with both C and H), and the organic composition excluding CH_4. In each category, a single ratio was calculated for each model hand fit; all together, six ratios were calculated in each category from the hand fits. These fits are shown in Fig. 2. Solar ratios (Asplund et al., 2009) are also shown for comparison. For the H/C ratio, these fits range between 2 and 3 for all orbits, nearly independent of the category (bulk versus organics versus non-methane organics) or the fitting endmember (ONS versus HC). The O/C ratios are slightly enhanced for Prox291 (0.1 to 0.4) across all categories as compared to Prox290 and Prox292 (0.1), which are equivalent to one another. Bulk N/C ratios for the ONS fits (0.1 to 0.2) are enhanced for all orbits compared to the HC fits (<0.1). Note that the HC fits do not include O or N in organics, and so the two fits cannot be compared in these categories. In all cases, the S/C ratio is zero within error. Although the inclusion of sulfur species contributes to the fit of certain regions of the mass spectra (e.g. H_2S for masses 32 u to 36 u), the resulting mixing ratios are very low. Alternatively, masses from 32 u to 34 u could plausibly be fit by phosphine (PH_3), which has previously been reported in Saturn's atmosphere (e.g. Fletcher et al., 2009).

The elemental ratios calculated from the auto fits were binned by frequency into 50 equally sized bins. Results are summarized as frequency curves in Fig. 2. The elemental ratios for the bulk composition from the auto fits span a broad range: from approximately 2 to 25 for H/C, from <1 to 6 for O/C, and from <1 to 10 for N/C. Organic distributions are less broad, but still show variation, especially for the H/C ratio, which ranges from 1 to 4. The O/C ratio ranges up to approximately 0.5,

Table 2
Top compounds in auto fits by mixing ratio. Note that mixing ratios are averaged over all fits in which the compound was included and are therefore not necessarily additive. The frequency refers to the fraction of all auto fits in which the compound was included.

	Compound	Formula	Average mixing ratio	Frequency
1	Hydrogen	H_2	0.999	1.00
2	Water	H_2O	3.6×10^{-4}	1.00
3	Helium	He	2.4×10^{-4}	1.00
4	Ammonia	NH_3	2.1×10^{-4}	0.39
5	Methane	CH_4	2.0×10^{-4}	0.66
6	Nitrogen	N_2	2.0×10^{-4}	0.36
7	Carbon Monoxide	CO	1.9×10^{-4}	0.36
8	Hydrogen Cyanide	HCN	6.9×10^{-5}	0.13
9	Formaldehyde	CH_2O	2.0×10^{-5}	0.12
10	Nitric oxide	NO	1.4×10^{-5}	0.17

Table 1
Summary of ten most abundant compounds in hydrocarbon and ONS hand fits.

	Hydrocarbon fits			ONS fits		
	Compound	Formula	Average mixing ratio	Compound	Formula	Average mixing ratio
1	Hydrogen	H_2	0.998	Hydrogen	H_2	0.998
2	Isobutane	C_4H_{10}	6.1×10^{-4}	Isobutane	C_4H_{10}	5.0×10^{-4}
3	Water	H_2O	3.6×10^{-4}	Water	H_2O	3.6×10^{-4}
4	Helium	He	2.4×10^{-4}	Helium	He	2.4×10^{-4}
5	Methane	CH_4	2.3×10^{-4}	Methane	CH_4	2.2×10^{-4}
6	Ammonia	NH_3	1.5×10^{-4}	Propargyl alcohol	C_3H_3OH	1.5×10^{-4}
7	Ethane	C_2H_6	5.8×10^{-5}	Ammonia	NH_3	1.5×10^{-4}
8	Propane	C_3H_8	5.4×10^{-5}	Nitrogen	N_2	1.2×10^{-4}
9	1-Hexyne	C_6H_{10}	5.0×10^{-5}	Hydrogen cyanide	HCN	5.3×10^{-5}
10	1,5-Hexadiene	C_6H_{10}	3.9×10^{-5}	Formaldehyde	H_2CO	3.8×10^{-5}

Table 3

Mass percentages for ring particles calculated from auto fits. All values are in weight percent of the ring material. Values have been adjusted to account for the fractionating effects of diffusion through Saturn's atmosphere. Totals are normalized to maintain the 37 wt% organic content reported in (Waite et al., 2018).

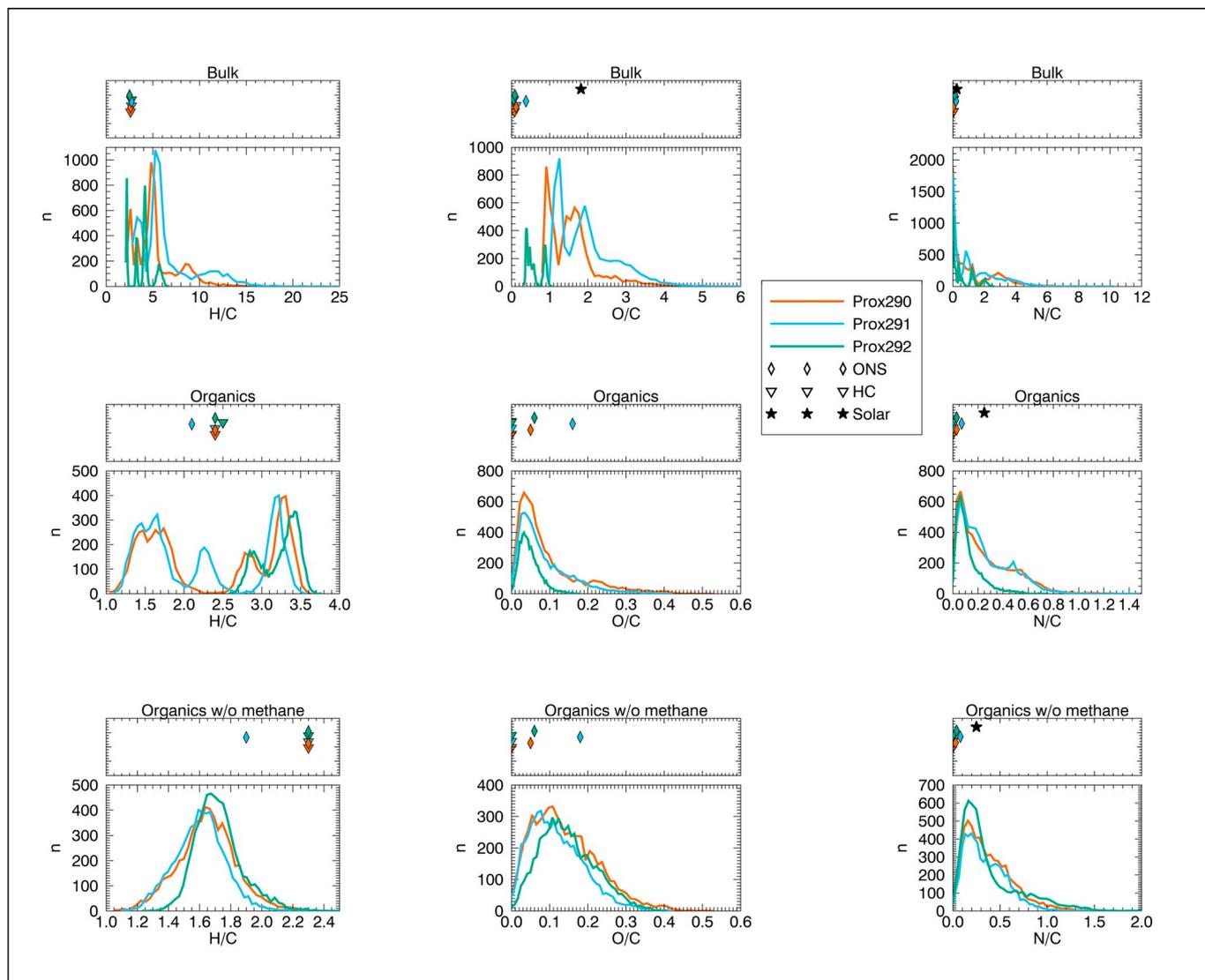|	CH_4	CO_2	CO	N_2	H_2O	NH_3	Organics*
This paper	9.0 ± 0.1%	0.4 ± 0.001%	15.7 ± 0.1%	16.4 ± 0.1%	17.9 ± 0.1%	3.6 ± 0.03%	37
Waite et al., 2018	16 ± 3%	0.5 ± 0.1%	20 ± 3%		24 ± 5%	2.4 ± 0.5%	37 ± 5%

Fig. 2. Elemental ratios for hand fits (symbols) and auto fits (lines) to integrated spectra shown in Fig. 1. The y-axis shows the number of auto fits corresponding to the elemental ratios for each curve. The symbols in the plots above share the same x-axis as the curves, but each symbol represents a single fit. The vertical offset of the symbols is for clarity only. Solar values are from Asplund et al. (2009).

and the N/C ratio extends as high as 1.4. With the exclusion of methane, the H/C distribution becomes much narrower, from 1 to approximately 2.4. The overall range of the O/C distribution does not change, but the peak becomes broader. The N/C range increases with removal of methane. The distribution of these auto fit ratios overlaps with the hand fit ratios, although in some cases the most frequent ratio differs from that calculated using the hand fit models.

2.3. Discussion

2.3.1. Fitting methodologies

Comparison of the hand fits and auto fits suggests that both methods have complementary strengths, and careful analysis within scientific context is required for interpreting the model fits. For example, the hand fit method allows adjustment of the abundance of a given compound as the model develops, which is presently not included in the auto fit methodology. The hand fits also give preference to compounds that have been selected as scientifically probable based on other environmental constraints, and may introduce some bias towards confirmation of previous results or expectations.

The auto fits allow a much more inclusive library to be tested, and the method is suitable for creating enough models to look for trends. However, the auto fit method is biased towards inclusion of compounds with fragmentation patterns that have few major peaks, regardless of the plausibility of their existence in the environment being sampled. For example, the noble gases had to be excluded from the auto fitting library

because each compound has only one peak, making them very weakly constrained. When noble gases were included, they were all identified in 100% of the fits despite the scientific improbability of the retention of such volatile, noble compounds in the ring material. This result reflected the inherent bias of the auto fitting method. We conclude that use of both hand fitting and auto fitting methods with careful comparison at the end is ideal.

2.3.2. Impact fragmentation

During the proximal orbits, the spacecraft velocity relative to the ring particles and co-rotating atmosphere was on the order of 30 km s^{-1}, equivalent to roughly 5 eV of energy per nucleon (Waite et al., 2018). Thus, material streaming into the INMS closed source had a high-energy interaction with the instrument antechamber wall prior to electron impact ionization in the closed ion source and subsequent mass analysis and detection. As a result, the possibility that some observed compounds could be products from impact fragmentation of larger organic compounds in the antechamber must be examined. Candidates for the larger compounds include the tholin-like materials that are suggested by remote observations (Cuzzi and Estrada, 1998; Cuzzi et al., 2018; Nicholson et al., 2008) or the 8000 u to 40,000 u particles detected by MIMI (Mitchell et al., 2018), which are not compositionally constrained by MIMI data but are spatially correlated with the INMS data (Perry et al., 2018; Waite et al., 2018).

Given that INMS measured volatile compounds with masses up to 99 u, it is clear that molecular fragments rather than atoms reached the INMS ion source. Studies of surface-induced dissociation suggest that ~25% of the energy of collision partitions towards internal energy of the molecule (de Maaijer-Gielbert et al., 1998). These experiments resulted in impact fragmentation of compounds into fragments with a range of masses (de Maaijer-Gielbert et al., 1998; Rakov et al., 2002). Experimental impact fragmentation studies of fragment abundance as a function of collisional energy indicate that while some fraction of the parent molecule may remain unfragmented at low impact energies (e.g. below 40 eV), at higher collisional energies the molecular abundance drops to negligible amounts (de Maaijer-Gielbert et al., 1998; Rakov et al., 2002). These results are supported by theoretical calculations of impact fragmentation, which suggest velocity-dependent fragmentation products (Vékey et al., 1995; Jaramillo-Botero et al., 2012). The three order of magnitude decrease in counts from $m/z = 10$–20 u to m/z = 90–99 u (Fig. 1) suggests that most of the molecular impact fragments produced were in the mass range measured by INMS, and higher masses only accounted for a small portion of the total fragments (Waite et al., 2018). The average pre-impact mass for the source material measured by INMS may be on the order of 200 to 500 u (see Section 3.2 in Perry et al., 2018).

The drop in INMS counts as a function of mass does not rule out the possibility that the fragments measured by INMS consisted of only the most labile components that broke off of larger residues, though. While the MIMI measurements of 8000 u to 40,000 u particles support the presence of heavier materials, MIMI reported a mass influx rate on the order of 5 kg/s (Mitchell et al., 2018), much lower than the 10^4 kg/s influx reported by INMS (Waite et al., 2018). This steep drop in influx rates (Perry et al., 2018) may suggest that the INMS data are representative of the major component of the inflowing ring material. However, it is possible that heavier materials that were invisible to INMS were present in the influx.

While impact fragmentation may be the source for the heavier compounds detected by INMS (100 u > m/z > 28 u), the spatial distribution for lighter compounds attributed to CH$_4$ and N$_2$ + CO differs from that of the heavier organics, suggesting different source populations (see Section 3). While CH$_4$ and N$_2$ + CO mixing ratios are constant at high latitudes, the heavy organics are depleted. This latitudinal dependence strongly suggests that the lighter compounds are not a product of impact fragmentation of the heavy organics. Instead, these compounds suggest the presence of latitudinally fractionated, volatile ring material.

2.3.3. Primary origin of compounds in the INMS antechamber

Although the latitudinal fractionation of the ring material supports the presence of light gases in the natural environment, it is important to consider whether these compounds could form inside the INMS antechamber. To test the probability of formation of a given type of bond (e. g. X-H, X-N, X-O), we consider the simplified case where all mass is present as atomic constituents, with the composition including both ring material and Saturn atmosphere calculated from the average of the hand fit model spectra. This average composition in molar percentage corresponds to 99.73% H, 0.01% He, 0.21% C, 0.03% O, 0.02% N, and negligible S.

A given tracer particle X should have ~120 collisions from the time it enters the INMS antechamber until it reaches the ionization region (Teolis et al., 2010); since molecules thermalize inside the chamber within the first couple collisions, this value is nearly independent of the spacecraft velocity. The coverage of external material on the antechamber walls is actually only a few percent, from our collision models of the antechamber. At the low densities found in the antechamber, these collisions should all be with the chamber walls (Teolis et al., 2010). As a conservative case, we instead assume that each of those 120 collisions is with an atom adsorbed to the instrument walls. We further assume that these adsorbed atoms have the average composition given above, which suggests that 119.7 of these collisions between the tracer particle and adsorbed atoms would be with an H atom, 0.2 collisions would be with a C atom, and the remainder would be with an N, S, or He atom.

Assuming a tracer population that has the same average composition given above for the adsorbed material, on the order of 10^{-6} out of 120 collisions would be between an N tracer atom and an adsorbed N atom, 10^{-4} out of 120 collisions would be between two C atoms, and ~10^{-4} out of 120 collisions would be between C and O. This suggests a very low probability for formation of heteroatoms or carbon chains via collisions in the antechamber, even assuming that each collision resulted in bond formation. (This is also improbable, since only those events that have both the required orientation for reaction and collisional energy that exceeds the activation energy will lead to bond formation.) Instead, 119 of these 120 collisions would be between two H atoms, suggesting that most collisions may simply result in formation of molecular hydrogen. The low rate of C—C collisions strongly suggests that compounds with masses >16 u are either endogenous to the ring material or are fragments of larger compounds endogenous to the rings. This is supported by the low frequency of C—C collisions estimated here (10^{-4}C-C collisions out of 120 total collisions gives a frequency of ~10^{-6}). The average mixing ratio for C$_2$H$_6$ from the hand fits is 4.5×10^{-5}, 1.5 orders of magnitude greater (Table S4). That of C$_3$H$_8$ is similar (4.3×10^{-5}), while the probability of a C$_2$—C collision should be much lower. We conclude that secondary formation of molecules in the antechamber via recombination is not a dominant process.

2.3.4. Identification of compounds

As expected, H$_2$ has a mixing ratio >0.99 in all spectra. The majority of H$_2$ is derived from Saturn's atmosphere, although a small contribution (<1%) is due to fragmentation of water and other H-bearing compounds. He, Saturn's other major atmospheric constituent, is consistently detected, although the mixing ratios are modest at these high altitudes [(2–3) × 10^{-4}]. The He mixing ratio at these altitudes, which differs from Saturn's bulk He mixing ratio, is comparable to the mixing ratios of other abundant compounds from the ring material, including water, methane, and ammonia.

Above the homopause where these data were collected, all masses >4 u are from infalling ring particles. While isobutane shows up in Table 1 with a higher average mixing ratio in the hand fits, this average is dominated by the organic-rich spectrum in Prox291. Isobutane mixing ratios range from 0 to 10^{-3} (see Table S4), and this variability as well as the low frequency of isobutane in auto fits indicates that isobutane is representative of an overall organic-rich composition but should not be

interpreted as a high abundance of isobutane specifically.

Water is therefore the most abundant single non-atmospheric compound, with a mixing ratio range of $(1–6) \times 10^{-4}$. Water comprises nearly 18% by mass of the infalling ring material measured by INMS (Table 3). However, remote sensing observations of the main rings have suggested a composition that is $\geq$80% by mass water (Clark and McCord, 1980; Pilcher et al., 1970; Poulet et al., 2003). Furthermore, near the ring plane, 70 to 90% of the larger charged particles detected by CDA (Hsu et al., 2018; Perry et al., 2018) were dominated by water ice (Hsu et al., 2018). INMS results therefore suggest a much lower relative abundance of water than the main rings or the material detected by CDA.

The INMS water abundance exceeds spectral modeling of the composition of the D68 ringlet (3–9% water by mass; Hedman and Stark, 2015). The spectral modeling fits, which assumed spherical ice particles, may underestimate the water abundance. The majority of the images used for this spectral modeling were captured before 2014, which is when the bright clumps in D68 became visible (Hedman, 2019). The increase in water content may therefore be related to exposure of fresh material. Alternatively, the INMS ring material is nanosized (Perry et al., 2018), which is smaller than the grain size distributions from the spectral modeling (Hedman and Stark, 2015); it is possible that the D68 material may be compositionally fractionated by size due to differences in the material strength of water and silicates, which were the other dominant component via remote sensing. The same material strength consideration could also apply to organics.

Volatile non-water species are dominated by organics, especially methane, which has a mixing ratio of $(2–3) \times 10^{-4}$. (INMS does not detect silicate grains or other refractory compounds that remain in the solid phase in the antechamber.) Also present in the model spectra (hand fits + auto fits) are NH_3 [$(0.9–2) \times 10^{-4}$], N_2 [$(0.03–2) \times 10^{-4}$], CO [$(0.002–2) \times 10^{-4}$], and CO_2 (3×10^{-9}–6×10^{-6}). Other notable compounds include glycine and methanol, which are both constituents of the model hand fit spectra but are not frequently included compounds in the auto fits. When fit separately to the spectra to remove contributions from other species and constrain the maximum abundance, the mixing ratios of glycine and methanol are still relatively low [$(2–6) \times 10^{-5}$ and $(0.7–4) \times 10^{-6}$ respectively]. In the case of glycine, the fit is constrained primarily by mass 75 u (as well as 46 u for Prox292), while methanol is constrained by 32 u. Upper limits for these compounds are provided in Table 4.

Masses above ~70 u were generally poorly fit by the model spectra. Signal at these high masses may include contributions from ionization fragments of parent species with primary masses that exceed the INMS mass range (up to 99 u). These compounds can be partially fit based on their fragments with masses <100 u; compounds used for the present

Table 4
Upper limits for selected compounds. These values are derived using only a partial fit to the spectrum. See Table S5 for further detail.

Formula	Compound	Mixing ratio upper limit and corresponding proximal
C_4H_{10}	Isobutane	1×10^{-3} (291)
H_2O	Water	7×10^{-4} (291)
CH_4	Methane	4×10^{-4} (291)
NH_3	Ammonia	3×10^{-4} (291)
CO	Carbon monoxide	3×10^{-4} (291)
N_2	Nitrogen	3×10^{-4} (291)
HCN	Hydrogen cyanide	2×10^{-4} (291)
H_2CO	Formaldehyde	1×10^{-4} (291)
C_4H_{10}	Butane	1×10^{-4} (292)
H_2NCH_2COOH	Glycine	6×10^{-5} (291)
C_6H_6	Benzene	8×10^{-6} (291)
CO_2	Carbon dioxide	6×10^{-6} (291)
CH_3OH	Methanol	4×10^{-6} (291)
O_2	Oxygen	2×10^{-6} (291)

work are listed in Table S2. However, the fits become increasingly degenerate as information about the molecular ion and heavier fragments is lost.

Overall, mixing ratios for individual compounds are very similar between the hand fits and the auto fits, suggesting robust values for the most abundant compounds that are independent of the fitting methodology used. Similarly, the mass percentages calculated for the ring material (Table 3) are generally in agreement with the values reported in Waite et al. (2018), with some exceptions. Mass percentages calculated in this work are more abundant for CO + N_2 than Waite et al. (2018) [32% versus 20%]. However, this is likely due to complete assignment of the 28 u peak to inorganic compounds in the auto fits used for this calculation, whereas Waite et al. (2018) assigned approximately 30% of 28 u counts to C_2H_4 based on constraints for CO and N_2 at 12 u and 14 u.

The attribution of a portion of the 28 u counts to organic constituents is consistent with the hand fit models. The N_2 and CO abundance ranges in the hand fits are $(0.032–1.4) \times 10^{-4}$ and $(0.023–7.1) \times 10^{-5}$ respectively (Table S4). The upper end of these ranges agrees with the auto fit average values of 2.0×10^{-4} and 1.9×10^{-4} for N_2 and CO. The lower end reflects contributions of organic compounds at 28 u. The weighted residuals for the hand fits are lower on average than those of the auto fits (<0.5 versus ~2), and the more complete assignment of counts in the hand fits may account for the increased organic attribution. The detection at high altitudes of 28 u (Perry et al., 2018; Waite et al., 2018) is likely due to this mixture of organic and volatile sources, with the more refractory organic components contributing to the equatorial offset of the counts from the density profile of the spacecraft orbit.

The lower abundance of water in the ring material in this work (Table 3) as compared to Waite et al. (2018) may be partially explained by the corresponding increase in NH_3, which leaves fewer residual counts at 17 u for the water fragment at the same mass. However, it is likely that organic ionization fragments in the auto fits further constrain water. This is consistent with the lower CH_4 abundance in this work, which may also be due to allocation in the auto fits of the 16 u and 15 u counts to NH_3 and organic compounds. We suggest that the true abundance of these compounds likely falls within the ranges shown in Table 3.

2.3.5. Elemental ratios

The interplay between CH_4 abundance and the abundance of other organics in the auto fits is also visible in the elemental ratios (Fig. 2). The H/C ratio of the organics displays clear populations of fits in all three proximals, with one population clustering between H/C = 3.0–3.5, and the other main population at H/C = 1.0–2.0. The first population suggests fits where CH_4 abundances dominate the 16 u counts, while the second may be related to fits in which the 15 u and 16 u counts are largely attributed to fragments from larger organics. There is a slightly higher frequency of fits with high methane abundance, and the different latitudinal distribution of methane with respect to higher masses (Section 3) still suggests the presence of methane as an abundant compound.

The broad range of bulk ratios in the auto fits in comparison to the hand fits is likely a product of the fitting methodology. The auto fits preferentially include light inorganic compounds such as NH_3 and N_2. On average, these fits only include approximately 30 compounds and have higher residuals than the hand fits. Therefore, organics, which are the main C-bearing compounds, are included at lower rates, resulting in H-, O-, and N-rich auto fit models. Broadening of the O/C and N/C peaks in the non-methane organics category is further illustration of this effect, and results from removal of C rather than addition of O or N. The visible shift to lower H/C ratio for Prox291 in both the organic and non-methane organic categories is consistent with the higher count rates for this orbit for masses >50 u (Fig. 1), and suggests a more organic-rich (i.e. C-rich) composition. This may be related to the longitudinal position of the orbit with respect to the D68 bright clumps (Hedman, 2019; Waite et al., 2018).

As discussed in Section 2.3.2, impact fragmentation of the ring

material was likely relatively efficient. However, if high-mass organic residues did remain unfragmented in the INMS antechamber, then the expected effect would be reported elemental ratios that are C-poor compositions relative to the true bulk material. The residues of complex organic material tend to evolve towards lower H/C, O/C, and N/C ratios when heated (i.e. C-rich residues), especially in the case of chondritic complex organics (Alexander et al., 2007). This fractionation occurs through release of more volatile compounds (Wu et al., 2004; Okumura and Mimura, 2011; see "van Krevelen diagrams" in Killops and Killops, 2013). Input of impact energy may result in similar chemical trends as those observed via input of thermal energy, leading to some elemental fractionation and enhancement of C in the hypothetical organic residues that were not measured by INMS. Alternatively, chemical changes on rapid impact timescales may be more likely to remove organic side-chains than slower, thermal processes. Qualitative examination of the recommended molecular structure for chondritic complex organics (Derenne and Robert, 2010), which may be closer analog material in the inner rings than tholins based on remote sensing models of the rings (Cuzzi and Estrada, 1998; also Section 1), suggests that the overall trend of enhancing C in the unmeasured residue may still be expected in this case. The constraints on the elemental ratios presented here, which are derived from the impact fragments and volatile components, could therefore be an upper limit.

2.3.6. Implications for origins and relationship to the main rings

Overall, the hand fits suggest the ring particles measured by INMS have depleted O/C, N/C, and S/C ratios relative to the solar values (Asplund et al., 2009). The auto fit elemental ratios include the possibility of solar ratios, although the most frequent ratios are still depleted. (The exception is the N/C ratio for non-methane organics, which agrees well with the solar ratio for the auto fits.) The D ring may be supplied by the C ring (Waite et al., 2018), which the model of Cuzzi and Estrada (1998) suggests is darker and less red relative to the A and B rings because the same volume influx of meteoroid impactors, which are enriched in carbon relative to the endogenous icy ring material, would have a larger effect on the more diffuse C ring than on the dense A and B rings. It is possible that an influx of similar particles has also enriched the C-content relative to the main rings of the D ring particles measured here. Such a mechanism would be expected to enhance the silicate content of the D ring as well. These refractory grains would not be detected by INMS, but may be consistent with the silicate nanograins measured by CDA (Hsu et al., 2018). The N/C ratio reported here overlaps with ranges reported for laboratory production of tholin films (but not grains) in simulated Titan conditions (Carrasco et al., 2016). Titan tholins have been used as spectral analogs to reproduce the red slope of Saturn's rings between 0.3 and 0.7 μm (e.g. Poulet and Cuzzi, 2002).

Previous searches of the A, B, and C rings in the near-infrared for non-water ices, including CH_4, CO, N_2, NH_4OH (hydrated ammonia) and methanol, did not identify spectral features associated with these compounds (Poulet et al., 2003). A possible feature from CH_4 was reported at 1.73 μm, but methane bands at 2.20, 2.31, and 2.37 μm were not detected (Poulet et al., 2003). Similarly, methane was not detected in remote sensing of the D ring (Hedman et al., 2007). Retention in the rings of highly volatile species like N_2, CO, and CH_4 on long time scales is not expected. To test the possibility of an endogenous origin, we approximated the diffusion of methane ice from the interior of a ring particle through a 2 m thick lag deposit for a 2 m thick methane ice layer using the method described in Schorghofer (2008) and vapor pressure values from Prydz and Goodwin (1972). Using temperatures between 50 and 100 K (Tseng et al., 2010; Filacchione et al., 2014), estimated porosities between 0.05 and 0.5, and tortuosity between 2 and 3 we find retention timescales on the order of thousands of years. We conclude that volatiles detected by INMS must have a geologically recent origin.

A more likely explanation than retention of volatiles in the rings may be collisional decomposition of refractory organics and/or deposition of

volatile material in the D ring. Alternatively, it is possible that collisional exposure of more refractory complex organics, followed by UV photolysis reactions (Baratta et al., 2019; Moores and Schuerger, 2012) or ion irradiation (Moroz et al., 2004) might produce more volatile compounds. Consideration of the time evolution of the bright clumps in the D68 ringlet suggests processing subsequent to collisions between ring material may be more likely than the introduction of exogenous material (Hedman, 2019).

3. Latitudinal dependence

While the final five orbits all had CA points at latitudes of approximately 6°S, Cassini's final plunge (Prox293) terminated at a latitude of 11°N. This configuration of orbits provides a unique opportunity to understand the degree of association between different compounds measured by INMS. We hypothesize that the Grand Finale dataset includes signal from two primary phases for ring components: gaseous volatiles such as CH_4 and solid nanograins (Waite et al., 2018). To test this hypothesis, we have compared data from Prox293 to Prox290, Prox291, and Prox292. Our assertion is that "volatiles," aka species that are in the gas phase and travel as molecules with total masses in the range of tens of amu, should be present at higher latitudes than nanograin species, which may travel in the solid phase as a conglomeration of different compounds with a subsequent mass on the order of thousands of amu or more (Mitchell et al., 2018). Therefore, if this hypothesis is correct, the mixing ratios of refractory compounds should be depleted in the final plunge relative to the other proximal orbits.

3.1. Data processing

For each orbit, we created an integrated spectrum that only included inbound data up to CA following the method outlined in Section 2.1. These inbound-only spectra provide a closer correspondence between Prox290-292 and Prox293, for which no outbound data exist due to Cassini's continued descent into Saturn's atmosphere. Since outbound data (which include the desorption tails from water, Fig. S1) were excluded, the absolute mixing ratios calculated from these analyses underestimate the water abundance; however, these analyses are effective for testing for qualitative differences between the two types of orbits.

We identified key tracer masses for six molecular categories. When possible, the highest-intensity ionization fragment mass was used. In some cases, interferences from other compounds required special processing or selection of a different mass, as noted below. The tracer masses used were: methane (15 u; water has an interference at 16 u), ammonia (17 u, which we modify by subtracting the 17 u ionization fragment from water), water (18 u), carbon dioxide (44 u), organics (56 u), and mass 28, which includes contributions from CO, N_2, C_2H_4, and fragments of other organics. For organics, we use 56 u as the tracer mass because it does not include contributions from inorganic fragments and has relatively high signal in all orbits.

While not strictly required for comparison of the proximal abundances, conversion from counts to densities gives an approximation of the mixing ratio. For this conversion, we use sensitivity factors ("s") listed in Table S2 for ammonia, water, and carbon dioxide, as well as the methane sensitivity factor in Table S2 scaled for 15 u. For both organics and mass 28, we use sensitivity factors that are linear combinations weighted by the abundances of the main contributing species as determined from hand fits of the integrated spectra (see Section 2). For 56 u [s = $(3.4 \pm 1.7) \times 10^{-4}$], these species are 2-propen-1-amine, 2-propenal, 1-hexene, and cyclohexene. For mass 28 (s = $6.4 \times 10^{-4} \pm 3.7 \times 10^{-7}$), we use a combination of N_2, CO, and C_2H_4. Conservatively, variation in sensitivity factors of compounds with molecular masses <100 u result in at most a factor of four difference in the calculated densities. While the sensitivity factors chosen have a minor impact on the absolute mixing ratios reported, the relative relationship between

orbits is not affected since the same sensitivity factors were used to process all four datasets.

3.2. Modeling of adsorption effects

In the comparison of mixing ratios for orbits that crossed the ring plane (Prox290-292) to the final orbit (Prox293), which did not cross the ring plane, only inbound data were used to make the data sets more similar. This data processing reduces the effects of adsorption, which depends on temperature, time, and surface coverage. However, the time duration of Prox293 is shorter than that of the other orbits used for comparison. Since the primary effect of adsorption is a time delay in detection of sticky species, this difference in duration could in effect still result in a reduction in the signal for sticky species compared to the inbound-only integrated spectra from Prox290-292. These sticky species include water and ammonia (Table S1), which are the two compounds that show the greatest apparent depletions in Prox293 (Fig. 3).

Therefore, to determine whether these depletions can be fully explained by instrumental effects or indicate real compositional differences, we used the Simulator for Chemical Reactions in A Mass spectrometer (SCRAM) (Bouquet, 2018). This model simulates the effects of adsorption and desorption of compounds inside INMS by tracking the time evolution of surface and gas populations. The surface population of compound i at each time interval τ is given by $N_{ad,i}$, equal to

$$N_{ad,i} = A\tau D_i(1-\theta)P_iJ_i\chi_i,\tag{1}$$

where A is the surface area of INMS, D_i is the sticking coefficient for compound i, θ is the fractional surface coverage, P is the partial pressure of compound i, and χ_i is the mixing ratio of compound i. We use a value of $\tau = 10^{-5}$ s throughout our simulations. J_i is given by

$$J_i = \frac{c_i}{4k_BT},\tag{2}$$

and is a function of the thermal speed (c_i) and temperature (T). Contemporaneous to calculation of the surface population, the gas population ($N_{des,i}$) is also tracked via the equation

$$N_{des,i} = -N_{ad,i}\nu_0\tau e^{\left(-E_{des,i}(1-\alpha\theta)/RT\right)},\tag{3}$$

where $N_{ad,i}$ is the number of adsorbed molecules of compound i. Desorption is dependent on the desorption energy of compound i ($E_{des,i}$) as well as the characteristic vibration frequency of the surface (ν_0). The value of E_{des} is itself a function of the surface coverage (θ), consistent with previous studies of the INMS antechamber properties (Teolis et al., 2010). Here, we vary the desorption energy as a Temkin isotherm. The Temkin factor α is between 0 and 1, with higher values indicating greater repulsion with increased surface coverage between adsorbed molecules. Values used in the present work are summarized in Table 5. The surface is assumed to be fully oxidized, so that the values chosen reflect interactions with TiO_2. Finally, for each time interval, the gas population is translated into counts following the equations described in Teolis et al. (2015), and the model output counts are compared to the INMS signal.

The input values for the model are the density as a function of time, calculated from INMS counts data using the method in Teolis et al. (2015), and the mixing ratios of the compounds of interest. Our initial mixing ratios were calculated by fitting the inbound-only integrated spectrum, as described in Section 2. These values were then adjusted and the model outputs reproduced in an iterative fashion to reduce differences between the model output and the measured counts.

3.3. Results

Inbound-integrated mixing ratios for Prox290 and Prox292 are

Table 5
Constants used in SCRAM model.

Variable	Description	Value	
A	INMS surface area	1.04×10^{-3} m^2	
τ	Time interval	10^{-5} s	
k_B	Boltzmann constant	1.38×10^{-23} m^2 kg s^{-2} K^{-1}	
T	Antechamber temperature	298.15 K	
ν_0	Surface vibration frequency[b]	10^{13} s^{-1}	

Variable	Description	Value, H$_2$	Value, CO$_2$
$E_{des, i}$	Desorption energy of species i	48,100 J mol^{-1} [a]	36,700 J mol^{-1} [c]
χ_i	Mixing ratio	0.99925737	1.65×10^{-6}
D_i	Sticking probability for compound i[c]	0.1	0.98
α	Temkin factor	0.50[b]	0.69[c]

[a] Brown and Buxbaum (1988).
[b] Estimated.
[c] Lin et al. (2012).

indistinguishable from one another in all six chemical categories explored (Fig. 3), consistent with the mass-by-mass comparison shown in Fig. 1. Prox291 has similar mixing ratios to the other full orbits (Prox290 and Prox292) for CH_4, 28 u, and CO_2. However, it is enriched in NH_3 and water relative to Prox290 and Prox292. Prox291 may also be organic-rich, which would be consistent with the increase in signal observed at high masses in Fig. 1. However, any increase in organic content relative to Prox290 and Prox292 still falls within the associated uncertainty.

Prox293, the final plunge at 11°N latitude that did not cross the equatorial plane, has the same mixing ratio of CH_4 and 28 u as the ring-plane-crossing orbits that have CA at 6°S latitude. However, the mixing ratios of NH_3, water, and organics are reduced relative to the full orbits. CO_2 may also be depleted in Prox293 relative to the full orbits, though the CO_2 data points are within uncertainty of one another.

To discriminate between instrumental and compositional effects, we used the SCRAM model (Section 3.2) to test the null hypothesis that all apparent differences between Prox293 and Prox290-292 were solely due to instrumental effects. If true, then modeling of the same input mixing ratios should produce equally good fits to the counts data for both Prox293 and a ring-plane-crossing orbit. We modeled two compounds: H_2, which was chosen as the dominant atmospheric constituent, and CO_2, which defines the cut-off between compounds with and without an apparent depletion in Prox293. H_2 was selected to represent non-sticky compounds, while CO_2 represents sticky compounds (see Table S1). To represent the ring-plane-crossing orbits, we selected Prox292 because it appears to have the lowest mixing ratios of those orbits. Therefore, testing for differences in CO_2 between Prox292 and Prox293 gives the most conservative result.

Model results are shown in Fig. 4. For both Prox292 and Prox293, H_2 has a mixing ratio >0.99 calculated from the data. The resulting H_2 counts profiles are reproduced well by the model output. The model output for CO_2 also reproduces the data in Prox292 well. However, the same input mixing ratio over-predicts the CO_2 counts compared to the data from Prox293. These results suggest that the modeled instrumental effects, namely adsorption and desorption inside INMS, do not fully explain the observed CO_2 depletion in Prox293. Were instrumental effects the only cause of the observed depletion, then the model output in Fig. 4d should match the data. Therefore, we reject the null hypothesis, and we conclude that there is a real compositional difference between Prox292 and Prox293.

This conclusion is supported by model outputs in Fig. 5, which show that when the CO_2 mixing ratio (Fig. 5d) or desorption energy (Fig. 5f) are adjusted to fit the INMS data from Prox293, the data in Prox292 are not fit (Fig. 5c and e). Based on the calculated χ^2 values for these models, the best fits for Prox292 and Prox293 are shown in Fig. 5a and f with CO_2 mixing ratios of 2×10^{-5} and 7×10^{-6} respectively. Since the difference
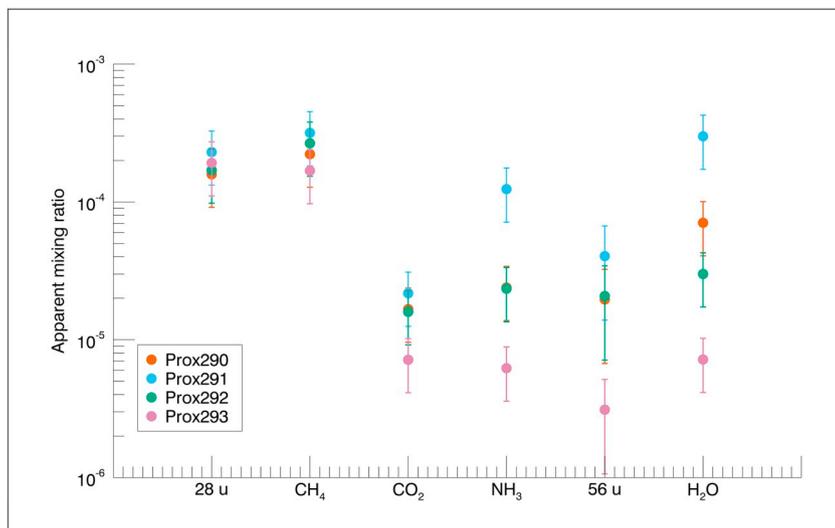
Fig. 3. Comparison of mixing ratios for orbits that crossed the ring plane (Prox290-292) and the final plunge (Prox293), which terminated at 11°N latitude. The final plunge is depleted in ammonia, water, and organics relative to the other orbits. Compounds are listed in order of decreasing volatility from left to right (see Fig. 7). Note that mixing ratios are approximate for two reasons: (1) adsorption effects can only be partially accounted for in Prox293, which does not have outbound data; and (2) sensitivities are estimated as described in Section 3.1. The analysis shown here is for the inbound-integrated spectra, and apparent differences for Prox290-292 from the mixing ratios in Tables 1 and 2 are due to adsorption effects.
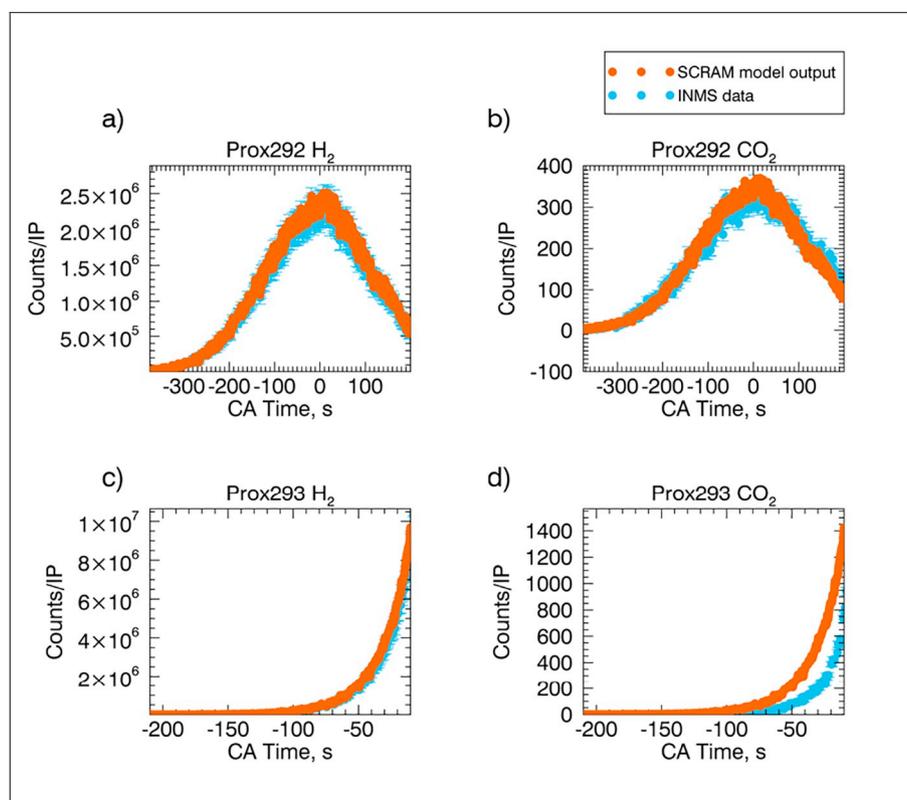
Fig. 4. Comparison of SCRAM model output using values in Table 5 with INMS data (shown with error bars) for Prox292 and Prox293. The model outputs reproduce both the H_2 (a) and CO_2 (b) data well for Prox292. For Prox293, the H_2 model outputs and data agree (c), but CO_2 data are depleted relative to the model outputs (d).

in CO_2 between Prox292 and Prox293 is the minimum difference observed of all the compounds compared in Fig. 3, we further conclude that the depletions in water and ammonia are also likely due to compositional differences at greater latitudes from the ring plane. Compositional differences are dependent primarily on latitude rather than altitude, as Prox293 is depleted in ammonia, water, and organics for altitudes below 2300 km (Fig. 6).

3.4. Discussion

The latitudinal extent of the compounds investigated here is correlated with volatility, suggesting that differences may be related to the presence of each compound in either the solid phase or the gas phase. Sublimation curves for pure species are shown in Fig. 7. For the range of pressures between the inner edge of the D ring ($\sim 10^{-10}$ bar) to the lowest altitudes for Prox290 through Prox292 (~ 1500 km, or 10^{-4} bar), CH_4 and mass 28 species (N_2 and CO) sublimate at much lower temperatures than CO_2, which may be depleted in Prox293, and NH_3 and water, which are depleted in Prox293. Curves for ethane (C_2H_6, 30 u) and benzene (C_6H_6, 78 u) are provided in Fig. 7 for comparison to the ring organics. Environmental conditions therefore favor sublimation of highly volatile compounds like CH_4, but not sublimation of more
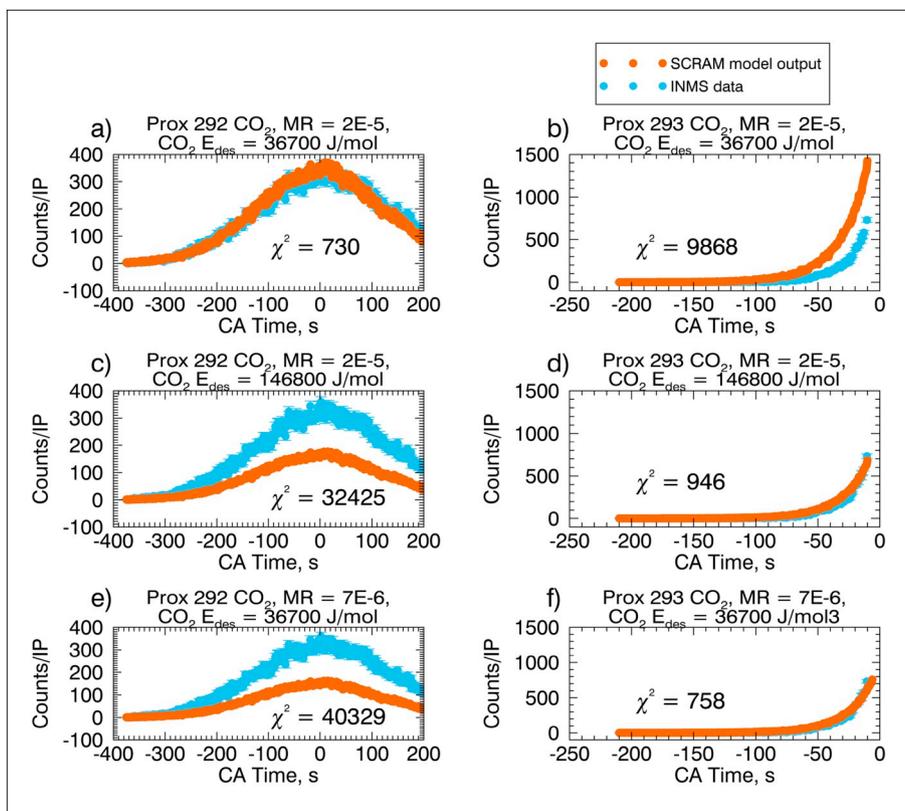
Fig. 5. Changes in the CO_2 mixing ratio (MR) or desorption energy to fit the INMS data from Prox293 result in poor fits for Prox292. χ^2 goodness-of-fit values are included for each model. Note that the degrees of freedom differ between Prox292 and Prox293 (331 and 172 respectively), and the χ^2 values should not be compared between the two proximal orbit datasets.

refractory compounds like CO_2. These results are consistent with our hypothesis that the ring material is comprised of both gas-phase and solid-phase components. CO_2 exhibits some depletion in Prox293 but still falls within the bounds of uncertainty, which further suggests that the division between volatile and refractory species in this context may be approximately the sublimation vapor pressure of CO_2. The gas-phase compounds may form part of the inner ring atmosphere (Johnson et al., 2006; Tseng et al., 2010), although the volatility of these compounds suggests they may be transient and related to collisions, as discussed in Section 2.3.6.

Our results can be used to infer the gas to dust molar ratio of the infalling material. From Fig. 3, we see that 28 u and CH_4 are primarily volatile. Making the simplifying assumption that 28 u and 15 u are completely volatile, the volatile mixing ratio is approximately 4×10^{-4}. CO_2, NH_3, organics (~56 u), and H_2O are the other most abundant compounds, and comprise the "dust" component. In this case, Fig. 3 shows that the dust mixing ratio is approximately 3×10^{-4}. This suggests a gas to dust ratio of the infalling material close to unity. The mixing ratios shown in Fig. 3 are not corrected for adsorption effects, and the preferred values are therefore in Tables 1 and 2. This distinction is less important for the volatile compounds defined here (28 u and 15 u), because these masses do not show strong adsorption effects. However, the "dust" component here is an underestimate for this reason. Performing a similar analysis on the auto fit average values, Saturn's atmosphere is defined as H_2 + He (Mixing Ratio, MR = 0.999). Inflowing gas is defined as methane, carbon monoxide, and nitrogen (MR = 5.94 $\times 10^{-4}$). The remaining compounds are defined as dust (MR = 7.98 $\times 10^{-4}$). This suggests a gas to dust ratio of 0.74. If this analysis is reframed slightly to consider a cometary context where CO_2 and H_2O would be volatile, then the result is a volatile/refractory molar ratio of 2.24. Since the INMS measurements of dust include only the fraction that was volatilized in the instrument antechamber, these estimates on the gas to

dust ratio are upper limits.

Previous results from the high-altitude and mid-altitude orbits suggested an offset from the atmospheric profile towards the equatorial plane for the 28 u counts (see Fig. 1 in Perry et al., 2018 and Fig. 4 in Waite et al., 2018). This has been interpreted as association of 28 u with larger nanoparticles rather than as gaseous molecules, which would be expected to couple with the atmosphere and therefore follow the same profile. The auto fits produced in this study (see Section 2) are consistent with contributions at 28 u from N_2 and CO, which are both volatile compounds (Fig. 7) that should couple with the atmosphere. However, the hand fits generated in this study suggest that approximately 30% of the low-altitude counts at 28 u may be due to organics based on constraints at 12 u on CO and at 14 u on N_2. These organic contributions may include C_2H_4 and ionization fragments of larger compounds. Therefore, this refractory component may lead to the previously observed high-altitude offset. Similarly, for 44 u the most probable fits are CO_2, C_3H_8, and organic fragments. The attribution to CO_2 is limited by the doubly-ionized peak at 22 u, which has very few counts in the spectra. This contributes to the relatively low CO_2 abundances reported in Tables 1 and 2. Attribution to organic compounds of a portion of the 44 u counts in the high-altitude data shown in Perry et al. (2018) would be consistent with attribution of a portion of the 28 u counts to an organic constituent.

4. Conclusions

During the Grand Finale, Cassini INMS made in situ measurements of material flowing in to Saturn's upper atmosphere from the D ring. These data reveal complex mass spectra, with signal across the full INMS mass range from 1 u to 99 u. Model fits to the data are consistent with an organic-rich composition, confirming earlier remote sensing spectral models that incorporate organics into ring particles in the main (A, B,
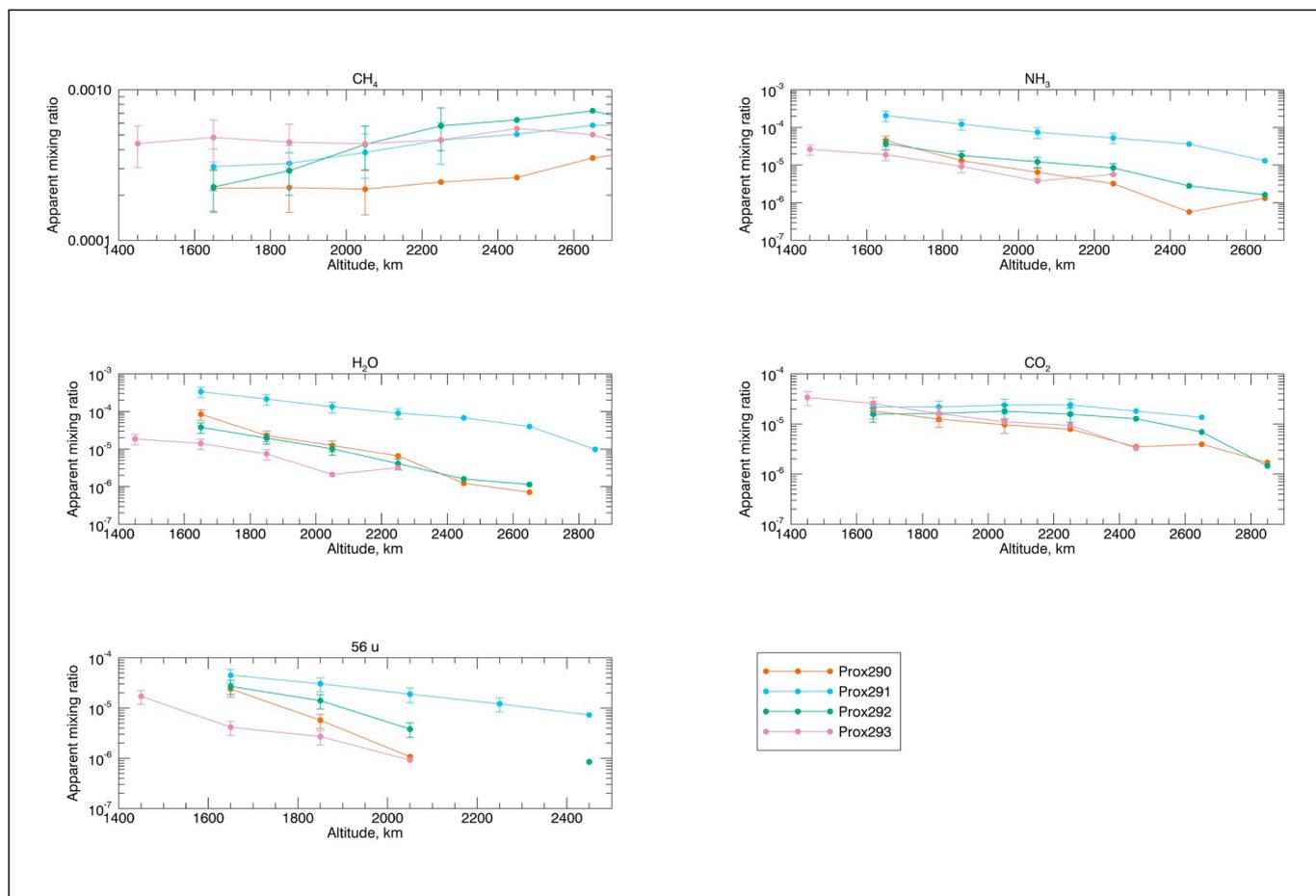
Fig. 6. Comparison of mixing ratios of CH_4, NH_3, H_2O, CO_2, and organics as a function of altitude. Values shown are for inbound trajectory only; apparent differences in mixing ratio for Prox290-292 from the values listed in Tables 1 and 2 are an artifact of adsorption effects.
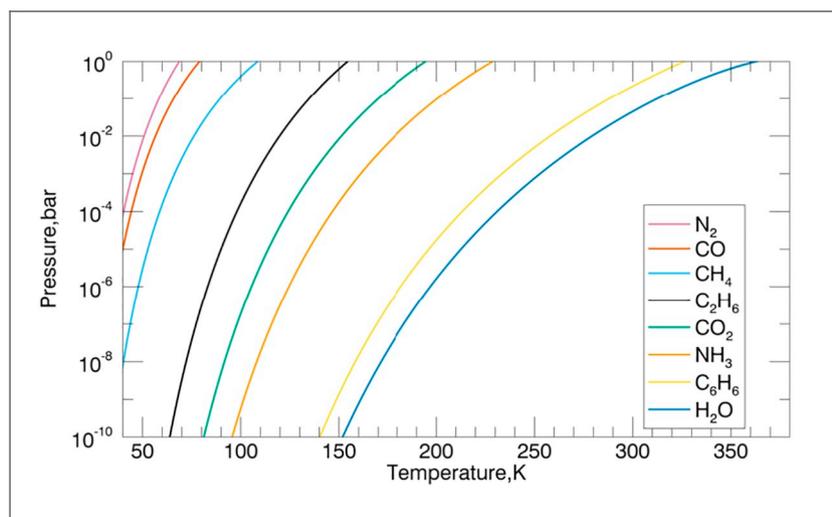

Fig. 7. Sublimation curves for pure compounds. Functions are taken from Fray and Schmitt (2009).

and C) rings (e.g. Ciarniello et al., 2019; Cuzzi et al., 2018; Filacchione et al., 2014; Hedman et al., 2013). These previous studies generally show an increase in non-icy material in the diffuse regions of the rings relative to the A and B rings, which may be consistent with relatively high organic abundances in the D ring relative to the bulk rings. However, these INMS results showing >70% by mass non-icy material exceed

remote sensing maxima. It is possible that the difference is related to exposure of fresh, relatively volatile material in the D68 ringlet, or to the small size of the particles measured by INMS (Perry et al., 2018). Ultimately, the reason for the high organic abundance remains an open question.

Our analyses confirm the abundances of CH_4, CO_2, CO, N_2, H_2O, and

NH$_3$ previously reported (Waite et al., 2018), suggesting that these values are robust and independent of the fitting method used. Comparisons to experiments suggest that most material that entered the INMS antechamber would have dissociated into molecular fragments; however, it is possible that some residues may have been too refractory for detection by INMS. Differences in the latitudinal distribution of light volatiles (CH$_4$, N$_2$, and CO) compared to heavier organics suggests that these compounds were endogenous to the ring material. Recombination in the instrument antechamber is rejected as an alternate method of forming these compounds. Elemental ratios calculated from these fits indicate that the D ring particles are C-rich relative to solar values, and especially depleted in S. The data support inclusion of some O- and N-bearing organics.

Latitudinal effects on the ring material composition indicate the presence of two phases: gaseous and solid material. This division is according to sublimation temperature, with the vapor pressure of CO$_2$ falling in between the two categories. Volatile material is enhanced relative to refractory material at latitudes away from the equatorial plane where the material is sourced. We calculate a gas to dust molar ratio for the ring material close to unity.

Acknowledgments and data

Appendix A. Supplementary data

Supplementary data to this article can be found online at https://doi.org/10.1016/j.icarus.2019.113595.

References

Acree Jr., W.E., Chickos, J.S., 2019. Phase transition enthalpy measurements of organic and organometallic compounds. In: Linstrom, P.J., Mallard, W.G. (Eds.), NIST Chemistry WebBook, NIST Standard Reference Database Number 69. National Institute of Standards and Technology, Gaithersburg MD, p. 20899. https://doi.org/10.18434/T4D303 (retrieved December 19, 2019).

Alexander, C.O.D., Fogel, M., Yabuta, H., Cody, G., 2007. The origin and evolution of chondrites recorded in the elemental and isotopic compositions of their macromolecular organic matter. Geochim. Cosmochim. Acta 71, 4380–4403.

Asplund, M., Grevesse, N., Sauval, A.J., Scott, P., 2009. The chemical composition of the sun. Annu. Rev. Astron. Astrophys. 47, 481–522.

Baratta, G., Accolla, M., Chaput, D., Cottin, H., Palumbo, M., Strazzulla, G., 2019. Photolysis of cometary organic dust analogs on the EXPOSE-R2 mission at the International Space Station. Astrobiology 19, 1018–1036.

Bouquet, A., 2018. Processes Affecting the Abundance of Astrobiologically Relevant Compounds From Icy Bodies Within the Solar System. Department of Physics and Astronomy, Vol. Ph.D. University of Texas at San Antonio, San Antonio, TX.

Brown, C.C., Buxbaum, R.E., 1988. Kinetics of hydrogen absorption in alpha titanium. Metall. Trans. A. 19A, 1425–1427.

Carrasco, N., Jomard, F., Vigneron, J., Etcheberry, A., Cernogora, G., 2016. Laboratory analogues simulating Titan's atmospheric aerosols: compared chemical compositions of grains and thin films. Planetary and Space Science 128, 52–57.

Ciarniello, M., et al., 2019. Cassini-VIMS observations of Saturn's main rings: II. A spectrophotometric study by means of Monte Carlo ray-tracing and Hapke's theory. Icarus 317, 242–265.

Clark, R.N., McCord, T.B., 1980. The rings of Saturn: new near-infrared reflectance measurements and a 0.326–4.08 μm summary. Icarus 43, 161–168.

Clark, R.N., et al., 2012. The surface composition of Iapetus: mapping results from Cassini VIMS. Icarus 218, 831–860.

Cuzzi, J.N., Estrada, P.R., 1998. Compositional evolution of Saturn's rings due to meteoroid bombardment. Icarus 132, 1–35.

Cuzzi, J.N., French, R.G., Hendrix, A.R., Olson, D.M., Roush, T., Vahidinia, S., 2018. HST-STIS spectra and the redness of Saturn's rings. Icarus 309, 363–388.

Derenne, S., Robert, F., 2010. Model of molecular structure of the insoluble organic matter isolated from Murchison meteorite. Meteorit. Planet. Sci. 45, 1461–1475.

Estrada, P.R., Cuzzi, J.N., 1996. Voyager observations of the color of Saturn's rings. Icarus 122, 251–272.

Filacchione, G., et al., 2014. Cassini–VIMS observations of Saturn's main rings: I. Spectral properties and temperature radial profiles variability with phase angle and elevation. Icarus 241, 45–65.

Fletcher, L., Orton, G., Teanby, N., Irwin, P., 2009. Phosphine on Jupiter and Saturn from Cassini/CIRS. Icarus 202, 543–564.

Fray, N., Schmitt, B., 2009. Sublimation of ices of astrophysical interest: a bibliographic review. Planetary and Space Science 57, 2053–2080.

Hedman, M., Nicholson, P., Cuzzi, J., Clark, R., Filacchione, G., Capaccioni, F., Ciarniello, M., 2013. Connections between spectra and structure in Saturn's main rings based on Cassini VIMS data. Icarus 223, 105–130.

Hedman, M.M., 2019. Bright clumps in the D68 ringlet near the end of the Cassini Mission. Icarus 323, 62–75.

Hedman, M.M., Stark, C.C., 2015. Saturn's G and D rings provide nearly complete measured scattering phase functions of nearby debris disks. Astrophys. J. 811.

Hedman, M.M., et al., 2007. Saturn's dynamic D ring. Icarus 188, 89–107.

Hsu, H.-W., et al., 2018. In situ collection of dust grains falling from Saturn's rings into its atmosphere. Science 362.

Jaramillo-Botero, A., An, Q., Cheng, M.-J., Goddard III, W.A., Beegle, L.W., Hodyss, R., 2012. Hypervelocity impact effect of molecules from Enceladus' plume and Titan's upper atmosphere on NASA's Cassini spectrometer from reactive dynamics simulation. Phys. Rev. Lett. 109, 213201.

Johnson, R.E., et al., 2006. Production, ionization, and redistribution of O2 in Saturn's ring atmosphere. Icarus 180, 393–402.

Killops, S.D., Killops, V.J., 2013. Introduction to Organic Geochemistry. John Wiley & Sons.

Lin, X., et al., 2012. Structure and dynamics of CO2 on rutile TiO2(110)-1×1. J. Phys. Chem. C 116, 26322–26334.

de Maaijer-Gielbert, J., Somogyi, A., Wysocki, V.H., Kistemaker, P.G., Weeding, T.L., 1998. Surface-induced dissociation of diphenyl ether. Int. J. Mass Spectrom. Ion Process. 174, 81–94.

Magee, B.A., Waite, J.H., Mandt, K.E., Westlake, J., Bell, J., Gell, D.A., 2009. INMS-derived composition of Titan's upper atmosphere: analysis methods and model comparison. Planetary and Space Science 57, 1895–1916.

Mitchell, D.G., et al., 2018. Dust grains fall from Saturn's D-ring into its equatorial upper atmosphere. Science 362, eaat2236.

Moores, J.E., Schuerger, A.C., 2012. UV degradation of accreted organics on Mars: IDP longevity, surface reservoir of organics, and relevance to the detection of methane in the atmosphere. Journal of Geophysical Research: Planets 117.

Moroz, L., et al., 2004. Optical alteration of complex organics induced by ion irradiation:: 1. Laboratory experiments suggest unusual space weathering trend. Icarus 170, 214–228.

Nicholson, P.D., et al., 2008. A close look at Saturn's rings with Cassini VIMS. Icarus 193, 182–212.

Okumura, F., Mimura, K., 2011. Gradual and stepwise pyrolyses of insoluble organic matter from the Murchison meteorite revealing chemical structure and isotopic distribution. Geochim. Cosmochim. Acta 75, 7063–7080.

Perry, M., et al., 2018. Material flux from the rings of Saturn into its atmosphere. Geophys. Res. Lett. 45, 10093–10100.

Perry, M.E., et al., 2010. Cassini INMS observations of neutral molecules in Saturn's E-ring. J. Geophys. Res. Space Physics 115.

Pilcher, C.B., Chapman, C.R., Lebofsky, L.A., Kieffer, H.H., 1970. Saturn's rings: identification of water frost. Science 167, 1372–1373.

Poulet, F., Cuzzi, J., 2002. The composition of Saturn's rings. Icarus 160, 350–358.

Poulet, F., Cruikshank, D., Cuzzi, J., Roush, T., French, R., 2003. Compositions of Saturn's rings a, B, and C from high resolution near-infrared spectroscopic observations. Astronomy & Astrophysics 412, 305–316.

Prydz, R., Goodwin, R.D., 1972. Experimental melting and vapor pressures of methane. J. Chem. Thermodyn. 4, 127–133.

Rakov, V.S., Denisov, E.V., Laskin, J., Futrell, J.H., 2002. Surface-induced dissociation of the benzene molecular cation in Fourier transform ion cyclotron resonance mass spectrometry. J. Phys. Chem. A 106, 2781–2788.

Schorghofer, N., 2008. The lifetime of ice on main belt asteroids. Astrophys. J. 682, 697.

Teolis, B., Perry, M., Magee, B., Westlake, J., Waite, J., 2010. Detection and measurement of ice grains and gas distribution in the Enceladus plume by Cassini's Ion Neutral Mass Spectrometer. J. Geophys. Res. Space Physics 115.

Teolis, B., et al., 2015. A revised sensitivity model for Cassini INMS: results at Titan. Space Sci. Rev. 190, 47–84.

Tseng, W.-L., Ip, W.-H., Johnson, R.E., Cassidy, T.A., Elrod, M.K., 2010. The structure and time variability of the ring atmosphere and ionosphere. Icarus 206, 382–389.

Vékey, K., Somogyi, Á., Wysocki, V.H., 1995. Internal energy distribution of benzene molecular ions in surface-induced dissociation. J. Mass Spectrom. 30, 212–217.

Waite, J., et al., 2004. The Cassini Ion and Neutral Mass Spectrometer (INMS) investigation. In: The Cassini-Huygens Mission. Springer, pp. 113–231.

Waite, J., et al., 2018. Chemical interactions between Saturn's atmosphere and its rings. Science 362, eaat2382.

Waite, J.H., et al., 2006. Cassini ion and neutral mass spectrometer: Enceladus plume composition and structure. Science 311, 1419–1422.

Wu, Z., Rodgers, R.P., Marshall, A.G., 2004. Two-and three-dimensional van Krevelen diagrams: a graphical analysis complementary to the Kendrick mass plot for sorting elemental compositions of complex organic mixtures based on ultrahigh-resolution

broadband Fourier transform ion cyclotron resonance mass measurements. Anal. Chem. 76, 2511–2516.

Zhang, Z., Hayes, A., Janssen, M., Nicholson, P., Cuzzi, J., de Pater, I., Dunn, D., 2017. Exposure age of Saturn's A and B rings, and the Cassini Division as suggested by their non-icy material content. Icarus 294, 14–42.

Zhang, Z., Hayes, A., Janssen, M., Nicholson, P., Cuzzi, J., de Pater, I., Dunn, D., Estrada, P., Hedman, M., 2017. Cassini microwave observations provide clues to the origin of Saturn's C ring. Icarus 281, 297–321.